Interfacial flow of a surfactant-laden interface under asymmetric shear flow

Eftekhari, M.; Schwarzenberger, K.; Heitkam, S.; Eckert, K.;

Originally published:

April 2021

Journal of Colloid and Interface Science 599(2021), 837-848

DOI: https://doi.org/10.1016/j.jcis.2021.04.126

Perma-Link to Publication Repository of HZDR:

https://www.hzdr.de/publications/Publ-32649

Interfacial flow of a surfactant-laden interface under asymmetric shear flow

Milad Eftekhari[1,2], Karin Schwarzenberger[1,2], Sascha Heitkam[1,2], Kerstin Eckert[1,2]*

[1]Helmholtz-Zentrum Dresden-Rossendorf, Institute of Fluid Dynamics, 01328 Dresden, Germany
[2]Technische Universität Dresden, Institute of Process Engineering and Environmental Technology, Germany

GRAPHICAL ABSTRACT

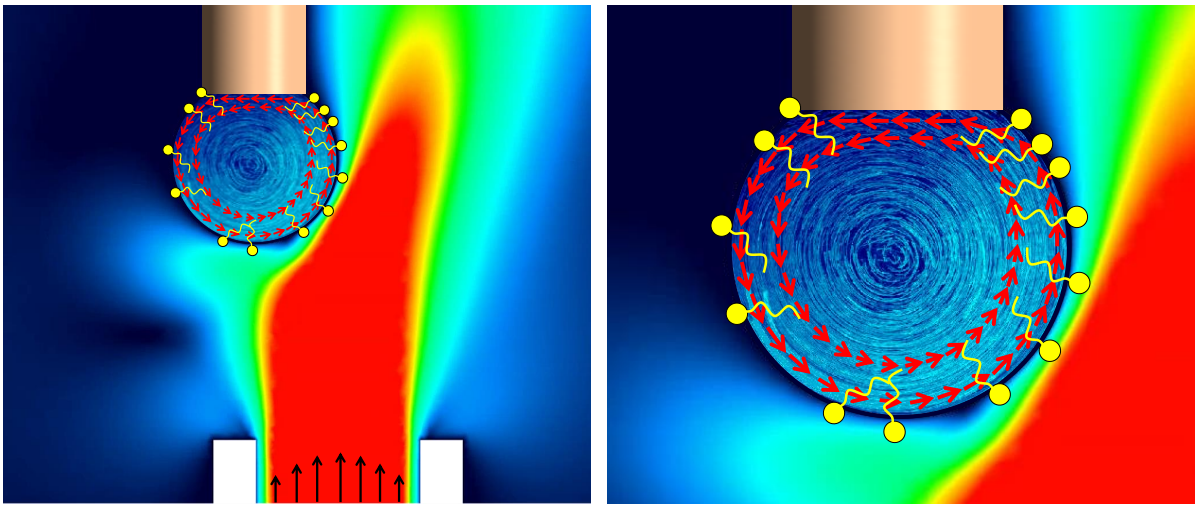

ABSTRACT

Hypothesis

The shear stress of the axisymmetric flow field triggers a nonuniform distribution of the surfactants at the surface of a rising bubble, known as stagnant cap. The formation of the stagnant cap gives rise to Marangoni stresses that reduce the mobility of the interface, which in return reduces the rising velocity. However, the conditions in technological processes usually deviate from the linear rise of a single bubble in a quiescent unbounded liquid. Asymmetric shear can act on the bubble surface e.g. due to the vorticity in the surrounding flow, bubble-bubble interactions, or influence of the reactor wall. A different surfactant distribution at the interface is expected under asymmetric shear, which can change the hydrodynamic behavior of the interface drastically.

Experiments

Here we conduct model experiments with a bubble or a drop at the tip of a capillary placed in a defined flow field. Thereby we investigate the influence of asymmetric shear forces on the interface in the presence of surfactants. Microscopic particle tracking velocimetry is employed to measure the velocity of the surfactant-laden interface for different degrees of asymmetry in the surrounding liquid flow.

Findings

We show a direct experimental observation of the circulating flow at the interface under asymmetric shear, which prevents the formation of the typical stagnant cap. Additionally, we reveal that the interface remains mobile regardless of the surfactant concentration. Our results confirm that increasing the degree of asymmetry increases the shear forces and thus the interfacial velocity.

1. Introduction

The adsorption of surface-active material at the interface changes the interfacial properties and boundary conditions, and hence the interfacial mass and heat transfer rates [1–3]. Typically, the adsorption process is considered instantaneous and the interface is supposed to be in equilibrium. Yet, in practice, surfactant molecules require some time to (i) diffuse to the interfacial sub-layer from the bulk phase, and (ii) to adsorb at the interface from the sublayer while (iii) adopting the favored orientation [4,5]. Thus, understanding the dynamics of surfactant adsorption at the interface is essential for the optimization and control of numerous industrial applications such as foams and emulsions, material processing, pharmaceuticals, and cosmetics [6–9]. Eastoe et al [10] and Miller et al [11] have provided a comprehensive review on the models developed to predict the equilibrium and time dependent surface tension of surfactant solutions. Many of these models assume the interface to be in quiescent condition. Yet, in view of technological applications, this assumption mostly does not hold as convection takes place in the surrounding bulk phase and at the interface. Therefore, in recent years, the emphasis has turned to moving interfaces and many studies have been carried out to understand the behavior of interfaces under dynamic conditions [8–11]. Particularly the interfacial dynamics of an air bubble rising in a liquid became an active research area [16–18] due to its high relevance to natural and industrial processes. It was shown that the surfactant adsorption rate [12] as well as its distribution at the interface [19] changes significantly in presence of flow. At the surface of a rising bubble, a nonuniform interfacial concentration distribution develops due to the surface advection caused by the main flow. The interfacial concentration gradient creates a tangential stress known as Marangoni stress, which opposes the shear stress of the flow [3]. At sufficiently high surfactant concentrations, the Marangoni stress retards the surface motion and thereby ceases the internal circulation known as Hadamard-Rybczynski flow [20]. The immobilization of the interface increases the drag coefficient towards that of a rigid sphere [21] and likewise forces the terminal velocity of the bubble to approach that of a rigid sphere [13,22,23]. To reflect the transition from mobile to immobile interface, the stagnant cap model is typically used in the literature. This simplified model divides the bubble interface in a fully immobile part at the trailing edge where the cap angle grows with increasing interfacial concentration, while the leading edge of the bubble remains mobile.

However, to describe the adsorption-desorption kinetics of a moving interface in more refined models, one needs to quantify the molar fluxes of the surfactant to and at the interface. This requires an accurate velocity measurement at the interface and its boundary layer, which would further allow a proper characterization of large variety of phenomena, such as bubble migration and accumulation, connected with the shear-induced lift force on bubble motion [24]. Even for a spherical bubble with clean surface rising in a linear shear flow, the influence of different parameters such as the Reynolds number, and the presence of walls leads to a nontrivial dependence of the lift coefficient [25]. In case of contaminated bubbles, the shear flow will also interact with the surfactant distribution on the interface, yielding additional complexity. Likewise, surface deformations, bubble-bubble interactions and Marangoni stresses at the interface lead to a high degree of

interaction that requires comprehensive experimental and/or numerical methods to identify the driving mechanisms and quantitative correlations. Takagi and Matsumoto [24] reviewed recent observations on the effect of adsorbed surfactants on the migration of bubbles in shear. Takagi et al [26] found that in the absence of surfactant, the bubbles tend to move toward the channel center. However, in presence of a small amount of surfactant, the bubbles tend to move toward the wall. They further confirmed that increasing the surfactant concentration increases the Marangoni stresses, so that the bubbles are shifted toward the center of the channel again. Due to the asymmetric shear forces acting in these cases, a surfactant distribution different from the symmetric stagnant cap model can be expected [27,28], which can change the boundary conditions around the bubbles significantly. As mentioned, a precise measurement of the velocity field would allow unraveling the above-described complex phenomena. However, the optical methods that are used to record the velocity distribution in the bulk fluids usually are lacking the spatial resolution to fully capture the boundary layer and thus the interfacial flow. Hosokawa et al. [15] evaluated the surface concentration profile of a falling drop using spatiotemporal filter velocimetry, giving access to the velocity field near the interface. Nevertheless, the interfacial velocity needs to be extrapolated from the closest velocities measured. This can introduce considerable uncertainties to the calculated data because of high velocity gradients in the boundary layer. Besides, such techniques are mostly limited to fluid-fluid interfaces since a high accuracy requires matching the refractive index of both phases.

In this study, direct experimental insights in the behavior of bubble and droplet interfaces under asymmetric shear forces are provided to address the above-sketched deficits. To that end, a reference flow is created around a stationary bubble placed at the tip of a capillary. This reference flow can be tuned with respect to the degree of asymmetry to impose different shear rates on the bubble surface. Particle image velocimetry (PIV) coupled with particle tracking velocimetry (PTV) is applied to characterize the flow around the bubble as well as on its surface. By tracking the adsorbed tracer particles, the interfacial flow can be captured with high spatial and temporal resolution. This method eliminates the uncertainty linked with the extrapolation of the boundary layer velocity, as the velocity at the interface can be directly measured by tracking the adsorbed particles movement at the interface. Profile analysis tensiometry (PAT) was conducted to study the interfacial properties of the employed surfactant. In combination with the measured velocities, the hydrodynamic shear stress on the interface is evaluated and further used to estimate the Marangoni stress, interfacial tension, and surfactant concentration distribution at the interface.

Our results indicate that the surrounding asymmetric velocity field creates a defined rotational flow at the bubble surface, which increases with the degree of asymmetry. This further changes the distribution of the surfactants at the interface. More importantly, our results demonstrate that under asymmetric shear flow, the interface remains *mobile* regardless of the concentration of the added surfactant. This phenomenon is expected to have significant influence on the hydrodynamics and mass transfer at bubbles with adsorbed material in various processes in chemical and minerals engineering.

2. Materials and methods

2.1. *Liquids*

Ultrapure water (Milli-Q ELGA, United Kingdom) with 18.2 MΩ resistivity and < 2 ppb organic content is used to prepare the aqueous solutions. Glycerol (CHEMSOLUTE, Germany) with a purity of ≥ 99.5% and silicone oil (Sigma Aldrich, Germany) were used to prepare refractive matched fluids.

In optical measurements, matching the refractive index of a two-phase system minimizes the distortions by the light refraction at the phase boundaries and hence increases the accuracy of the measurements [29]. Liquid-liquid combinations with a refractive index around 1.4 are commonly used in the literature, as this value is easy to implement for several aqueous-organic systems by adding the corresponding amount of glycerol to water. For the silicone oil used in this study, a matching refractive index between both phases was found at 49.3 wt% glycerol. A digital laboratory refractometer (LR-01, Maselli, Italy) was employed to measure the refractive index of the employed liquids accurately. Table 1 shows the physical properties of the pure liquids and the water-glycerol mixture.

Table 1. *Liquids used in experiments, with their refractive index, density, and viscosity at room temperature.*

	Water	Glycerol	Silicone Oil	Water-Glycerol
Refractive index	1.33272	1.47240	1.39629	1.3959
Density ($kg \cdot m^{-3}$)	998	1231	913	1125*
Dynamic viscosity (mPa·s)	1.04	1420	4.6	4.9*

* the values are adopted from Sheely et al [30].

2.2. *Surfactants*

Sodium dodecyl benzene sulfonate (SDBS, anionic surfactant) with a purity of ≥ 99% was used as purchased (Merck, Germany). The anionic surfactant was chosen to avoid unwanted hydrophobization of the tracer particles for the flow measurements, which would be expected in the case of cationic surfactants due to the electrostatic adsorption of cationic surfactants on the negatively charged surface of the particles [31]. The critical micelle concentration (CMC) value of SDBS was determined by surface tension measurements. The results provided a CMC value of 2.2 mM, which is in good agreement with the literature value [32].

2.3. *Surface tension*

Profile analysis tensiometry (PAT-1M, Sinterface Technology, Germany) was used to evaluate the dynamic surface tension of the employed solutions. The principle of measurement is described in detail in [32]. Briefly, a drop is created at the tip of a stainless-steel capillary. The pear-shaped profile of the pendant drop is defined by the interaction of interfacial tension and gravity. Using image processing, the droplet profile is determined and fitted by the Gauss-Laplace equation and from that, the interfacial tension is obtained.

2.4. *PIV measurements*

Particle image velocimetry (PIV; LaVision, Germany) was applied to measure the flow around the bubble and on its surface. PIV is an optical technique to measure the velocity field in a fluid that is seeded with sufficiently small and neutrally buoyant tracer particles. Polystyrene (PS) particles (microParticles GmbH, Germany) with a diameter of 5.06 µm, a density of 1020 $kg \cdot m^{-3}$ and an incorporated fluorescent dye (rhodamine; red fluorescent: excitation and emission at 530 nm resp. 607 nm wavelength) served as tracers. At low Stokes numbers, the particles follow the movement of the fluid perfectly [33]. The Stokes number for the particle-laden flow around the bubble is defined as:

$$\mathrm{St}=\frac{\rho_\mathrm{p} D_\mathrm{p}^2 u_\mathrm{Max}}{18\mu_f D_\mathrm{b}} \tag{1}$$

where ρ_p is the density of the particle, D_b and D_p are bubble and particle diameters, respectively, u_Max is the maximum velocity present within the system (for a conservative estimation), and μ_f is the dynamic viscosity of the fluid. The Stokes number in our case was $\mathrm{St} \simeq 0.01 \ll 1$ suggesting the high ability of the particles to follow the flow. Excited by a Nd-YLF laser (Photonics Industries, USA), the fluorescent particles emit light that is separated from the background scattered light of the laser by an optical long-pass filter. Thereby, mainly the particle signal is captured by the high-speed camera (Phantom VEO 410L, 1280 × 800 pix, AMETEK, USA) via a Zeiss Stereo microscope with PlanApo S 1.0× objective (Zeiss, Germany), used at 3.2 x zoom level. These optical parameters yield a spatial resolution of ~250 px/mm. The temporal resolution of the high-speed camera was set to 200 fps. Due to the confocal optics, the tracer particles are imaged sharply in a quasi-2D measurement plane (depth of field 0.18 mm) while the blurred signals outside the measurement plane do not contribute to the evaluation algorithm. This algorithm divides the recorded images in discrete interrogation windows that set the spatial resolution of the vector field. The movement of the tracer particles in the interrogation windows is determined from the cross-correlation of two consecutive images. This relatively coarse velocity field serves as a predictor for the velocity distribution. Subsequently, particle tracking velocimetry (PTV) is applied as post processing to individual tracer particles to achieve higher spatial resolution within the interrogation window (PIV evaluation software DaVis, LaVision, Germany) [34]. PTV was also employed for tracer particles adsorbed on the bubble surface to study the interfacial flow.

The setup to create the flow around a bubble is similar to that reported previously by Lotfi et al [12]. A cuvette with a cross-sectional area of 30×30 mm^2 and a height of 30 mm was mounted on top of a translation stage (labelled in Fig. 1a). As shown by the detail in Fig. 1b, the bubble was formed at the tip of a straight capillary (outer diameter 1.2 mm) using a micro syringe (for this precise dosing, the volumetric control of the afore-mentioned PAT-1M device was also utilized here). A steady liquid flow from the bottom to the top of the cuvette was generated using a U-shaped capillary of ~2 mm inner diameter as a nozzle which was connected to a syringe pump (Ascor med, Poland; labelled in Fig. 1a). The composition of the inflowing liquid is identical to the liquid in the cuvette. The vertical distance between the inlet nozzle and the bubble was set to Δh = ~7 mm. The end part of the U-shaped capillary points vertically towards the bubble center and can be shifted in

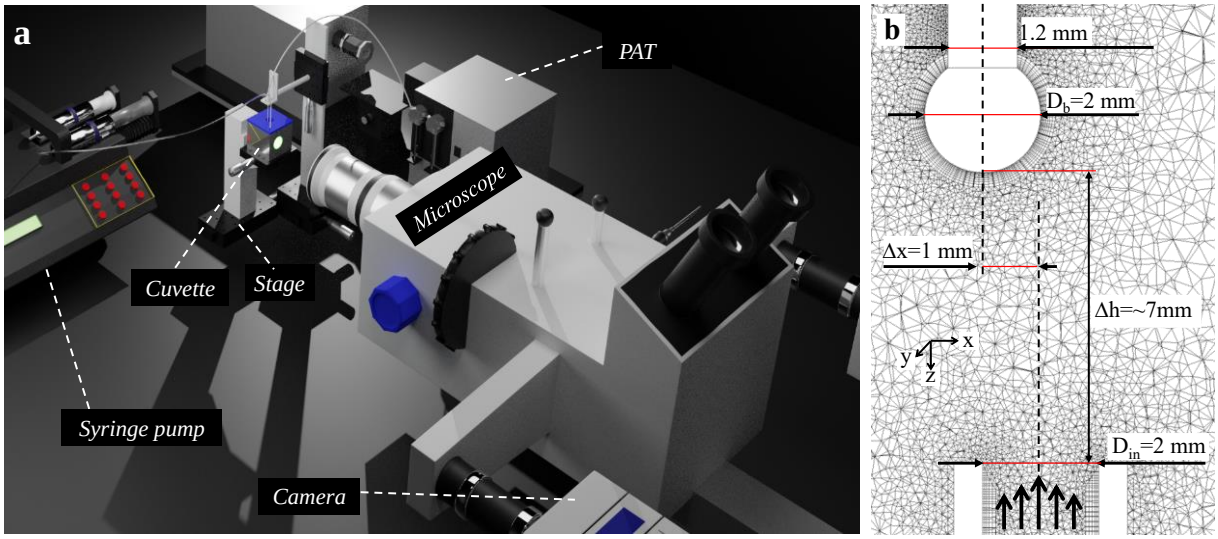

Figure 1. a) Stereo PIV setup to measure the velocity field. b) Mesh used for the simulations inside the *cuvette* (a) together with definition of the geometry with a bubble at the end of a capillary placed above the flow of the inlet nozzle.

x-direction by means of the translation stage, setting a horizontal distance of Δx between the centerline of the bubble and that of the inlet nozzle (cf. Fig. 1b). For laminar flow inside a pipe, the entrance length (L_e) can be calculated using equation 2:

$$\frac{L_e}{D_{in}} = 0.06\,\mathrm{Re}_{pipe} \approx 1.8 \qquad (2)$$

where D_{in} is inner diameter of the pipe, and Re_{pipe} is the Reynolds number of the flow inside the pipe. The straight end part of the U-shaped capillary in our experiments was more than $2D_{in}$; hence, a fully developed flow is expected inside the inlet nozzle.

2.5. *Numerical simulations*

3D numerical simulations of the flow field around a bubble placed on the tip of a capillary were carried out using the *commercial software* ANSYS CFX. It solves the unsteady Navier-Stokes equations on structured or unstructured meshes employing the finite volume method. The numerical setup and the mesh are shown in Fig. 1b. Due to the low bubble Reynolds number of approximately 20, a steady-state isothermal simulation without turbulence modeling is performed. Around the bubble, an inflation layer with radial resolution equal to 10^{-5} m=0.01 R_b and growth rate, equal to 1.2 was generated. The growth rate represents the increase in mesh size with each succeeding layer, starting from a defined face, in this case the bubble surface. For example, a growth rate of 1.2 results in a 20% increase in mesh size with each succeeding layer. A constant mass flow rate was imposed at the inlet. The same mass flow rate was set at the upper boundary to mimic a rising water level. The bubble surface adopted either a boundary condition with no-slip and zero velocity (corresponding to a solid sphere) or free-slip (corresponding to a perfectly clean bubble), while all other boundaries were kept no-slip. Additionally, the bubble surface is assumed undeformable in numerical studies, which is line with the experimental observation, i.e. absence of

deformations at employed flow rates. Indeed, in higher flow rates, the bubble deformation due to the dynamic pressure from the flow needs to be considered. A mesh sensitivity analysis was performed to check the convergence of the simulations. The results showed that the velocity magnitude close to the bubble surface changes in average less than 1% by doubling or halving the grid size. For this estimation, the velocity magnitude variation at 100 points is considered, which were homogenously distributed between R and $1.25R$. Additionally, the net torque on bubble surface changed less than 1% by changing the mesh.

3. Results and discussion

3.1. *Surface tension*

To characterize the interfacial properties of the employed surfactant SDBS, the equilibrium surface tension values are measured as a function of surfactant concentration using the pendant drop method (PD). Fig. 2a shows the obtained isotherm for SDBS. The isotherm is used to calculate the amount of adsorbed material at the interface, the CMC value, and the partial molar area of the surfactant [32,35,36] which will be needed in Sec. 3.4. Indeed, it would appear more logical to use a buoyant bubble (BB) instead of a PD to have better analogy with the previously described PIV setup. However, because of the following practical advantages the PD method is employed. The fitting of the buoyant bubble profile to the Gauss-Laplace equation (cf. Sec. 2.3) is more challenging due to the accuracy limit on the edge detection of a bubble image [37,38]. More importantly, the BB technique is much more susceptible to the influence of impurities within the system due to the direct contact of the studied liquid with the container. On the other hand, PD normally delivers a higher equilibrium surface tension values at the same surfactant concentration because of the known depletion effect. Due to the limited amount of surfactant available in the droplet volume, the bulk concentration of the system decreases as the surfactant adsorbs at the interface [39]. The depletion effect can be quantitatively addressed via a mass balance:

$$c = c_0 - \left(sur/vol\right)\Gamma \tag{3}$$

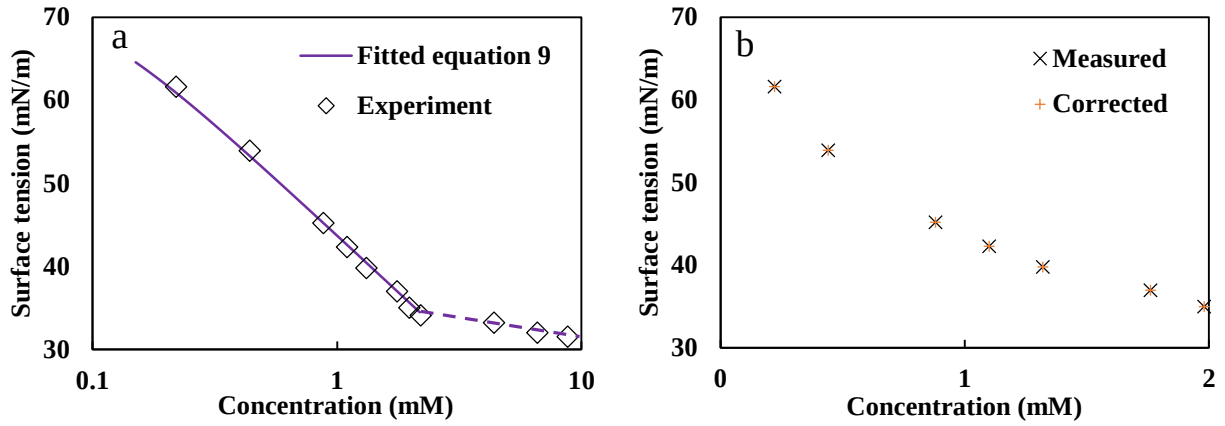

Figure 2. a) Equilibrium surface tension as a function of SDBS concentration measured using the pendant drop method (PD). The dashed line for C > 2.2 mM is drawn as guide for the eye. b) Comparison between the measured and corrected isotherms for SDBS considering the depletion effect.

where c and Γ are the bulk and surface concentration of the surfactant, respectively, *sur* is the area of the interface, and *vol* is the volume of the phase that contains the surfactant. The second term at the right-hand side of equation 3 expresses the concentration decrement in the bulk due to the surfactant adsorption.

As can be inferred from equation 3, the depletion effect is much more prominent for the PD method as the surface area to volume ratio is much higher compared to the BB method. Therefore, the PD results were corrected using equation 3 and the corrected values are plotted in Fig. 3b. As one can see from this figure, the surface tension values are almost identical for the employed surfactant and the depletion effect can be neglected.

3.2.*Flow field around the bubble*

Flow-on-bubble experiments allow exerting a defined shear on the bubble surface merely by shifting the relative position of the bubble to the inflow jet. Additionally, this setup allows adjusting relevant parameters independently, such as bulk velocity, bubble size, and surfactant concentration. In rising bubble experiments, by contrast, the terminal velocity at constant bubble size decreases with increasing surfactant concentration [40]. For our experiments, a defined and reproducible flow field was generated using the setup depicted in Fig. 1. The volumetric flow rate was set to 150 $mL \cdot h^{-1}$ corresponding to a bulk velocity of ~13.3 $mm \cdot s^{-1}$ directly at the nozzle outlet. The flow measurements were carried out in an aqueous solution containing different concentrations of SDBS, varied the range of 0.22 mM to 8.8 mM. However, no clear effect of the surfactant concentration on the flow pattern was observed for the range of surfactant concentrations employed in this study. Hence, we focus on a concentration of 2.2 mM, corresponding to CMC, and provide exemplary results throughout the whole concentration range in the SI (cf. Figure S1). This high surfactant concentration was chosen (i) to account for the large amount of surface-active materials present in many industrial processes and (ii) to minimize the influence of unwanted impurities from setup parts and/or the surrounding atmosphere. It is worth mentioning that a slight dissolution of the fluorescent dye from the PS tracer particles already can introduce a certain degree of contamination to the system, which can affect the interfacial hydrodynamic properties of an otherwise pure system [41]. It should be noted that the bubble surface reaches the equilibrium quite fast for concentrations around CMC. Additionally, the presence of flow significantly increases the adsorption rate [12] and one can assume that the interface has approached equilibrium in the time between switching on the flow and starting the PIV measurement.

Because of the rather specific geometry of the studied system, the velocity field is thoroughly characterized by a combination of PIV measurements and numerical simulations on a similar setup (cf. Fig. 1b). The simulations further allow estimating 3D parameters of the flow such as the total torque on the bubble surface. Fig. 3 compares the numerical no-slip (a,c) and experimental (b,d) results for a bubble placed centered (a,b) and off-centered (c,d) with respect to the inlet nozzle for 2.2 mM of SDBS. The experimental data is time-averaged over 2 s. In the case of a symmetric flow around the surfactant-laden bubble, a stagnation point on the leading edge and a pronounced wake (blue region of low velocity) on the trailing edge of the bubble are visible. Since the nozzle provides a jet rather than a homogeneous flow field, the flow is forked by the bubble, leading to an earlier detachment of the flow at the bubble perimeter and a more prominent wake. Rising bubbles present

a concentration gradient of adsorbed substances along their surface due to the surface advection caused by the main flow. Such a nonuniform distribution of surfactants causes a surface tension gradient that triggers a Marangoni stress opposing the shear stress of the flow. An analogous effect might be expected for a bubble on the tip of a capillary placed in a symmetrical flow. In this case, a surfactant rich area would develop close to the capillary and a "clean" interface at the leading edge of the bubble. In Fig. 3, the experimental results are reproduced well by the simulations with a no-slip bubble surface. This is indicated by the regions of near-zero velocity adjacent to the bubble surface in the experiment which are absent for a free-slip surface (cf. SI, Figure S2). Since a similar flow field was obtained for all employed surfactant concentrations, we conclude that a no-slip boundary condition was reached in each case. This agrees with the observations from Hosokawa et al [2,15] who have reported a nearly retarded interface in presence of only 0.036 CMC, i.e. 10^{-2} mM of a Triton surfactant.

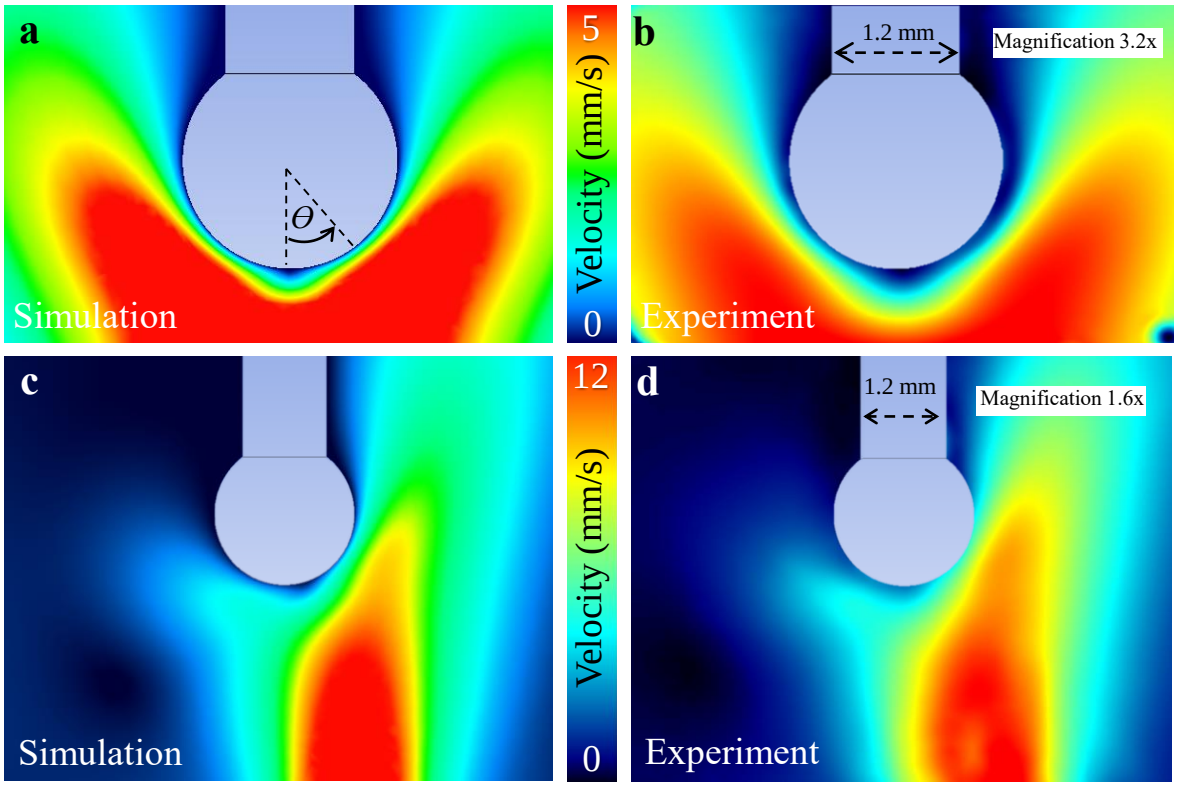

Figure 3. Velocity distribution around a bubble attached to the tip of a capillary for experiments with 2.2 mM SDBS and simulations with no-slip surface boundary condition. a,c) Simulation (ANSYS, steady state) and b,d) experiment (time-averaged over 2s); a,b: 3.2 x magnification and symmetric position with respect to inflow; c,d: 1.6 x magnification with 1 mm asymmetric position (Δx according to the definition in Fig. 1b).

To study the behavior of the bubble surface under asymmetric shear, we now shift the bubble in horizontal direction (cf. Fig. 1b). Thus, the center of the inflow with maximum velocity is located at the bubble side, here with a displacement of 1 mm. The good agreement between the flow pattern of the experiment and the simulation again suggests that the system yields a flow boundary

condition that is close to no-slip (cf. Fig. 3 c,d). However, the region with zero velocity adjacent to the bubble surface is not clearly visible at the right-hand side of the experimental velocity field. This can be attributed to experimental uncertainties or the existence of a slow interfacial flow in the asymmetric case, which can also cause a certain deviation from the theoretical no-slip case.

3.3.*Interfacial flow on the bubble surface*

The response of the interface to the asymmetric shear flow is studied by tracking the adsorbed PS particles at the bubble surface (example videos V1.mp4 and V2.mp4 in SI). Fig. 4a illustratively shows how the adsorbed particles move in response to the asymmetric shear flow. The bulk velocity difference between the left and the right side of the bubble drives a rotational surface flow. This surface flow is aligned with the bulk flow on the right side, where the bulk velocity is higher. On the left side of the bubble, where the bulk flow is slower, the interfacial flow opposes the bulk flow direction by pointing downwards. Irrespective of the interfacial flow, one might argue that the particles are dragged upward by viscous forces on the right-hand side and move downward on the left side by inertia. However, the negligible density difference between the PS particles and the aqueous solution as well as the low particle Stokes number (equation 1) demonstrate that the particles should follow the streamlines of the flow nearly perfect. Consequently, inertia effects cannot explain the movement of the PS tracers. To reconstruct the three-dimensional movement of the PS particles, we use the information that the PS particles are bound to the interface. By describing the bubble surface as a spheroid (equation 4), the out of plane component of the velocity V_y can be derived from the position (x, z) and velocities (V_x and V_z) of the two-dimensional images. Since the velocities in x and z direction are both known from the PTV evaluation, the third velocity component is calculated according to equation 5.

$$\frac{x^2}{a^2}+\frac{y^2}{a^2}+\frac{z^2}{b^2}=1 \tag{4}$$

$$V_y=-\frac{xV_x+\frac{a^2}{b^2}zV_z}{y} \tag{5}$$

An example for the obtained 3D path of a well-visible cluster of PS particles is shown in Fig. 4a and b where the velocity of the cluster approximately represents the interfacial velocity. Interaction and agglomeration of the adsorbed tracer particles certainly influence the direct coupling of the particle movement to the interfacial flow. However, the phenomenon of rotating flow remains unchanged when the seeding with tracer particles is sparser.

The velocity components normalized by the inlet velocity are plotted in Fig. 4c-e over the angular position θ (defined in Fig. 3a). The depicted particle path starts at $\theta \approx$ -40° (start position marked green) and after approx. 0.5 seconds, the particles reach the leading edge of the bubble ($\theta = 0°$). Driven upwards by the surface flow, they approach the position of the capillary. Like a two-dimensional flow around a cylinder, the capillary poses an obstacle and a stagnation zone forms in front of the capillary. Consequently, all velocity components strongly decrease near the capillary $|\theta| > 140°$. Thereafter, the particles either can be trapped in the stagnation zone to form a large stationary particle agglomerate or – depending on their position – are reaccelerated to another

circulation on the bubble surface. Additionally, the circulating movement is disturbed by the needle resulting in a redistribution of the particles on the surface.

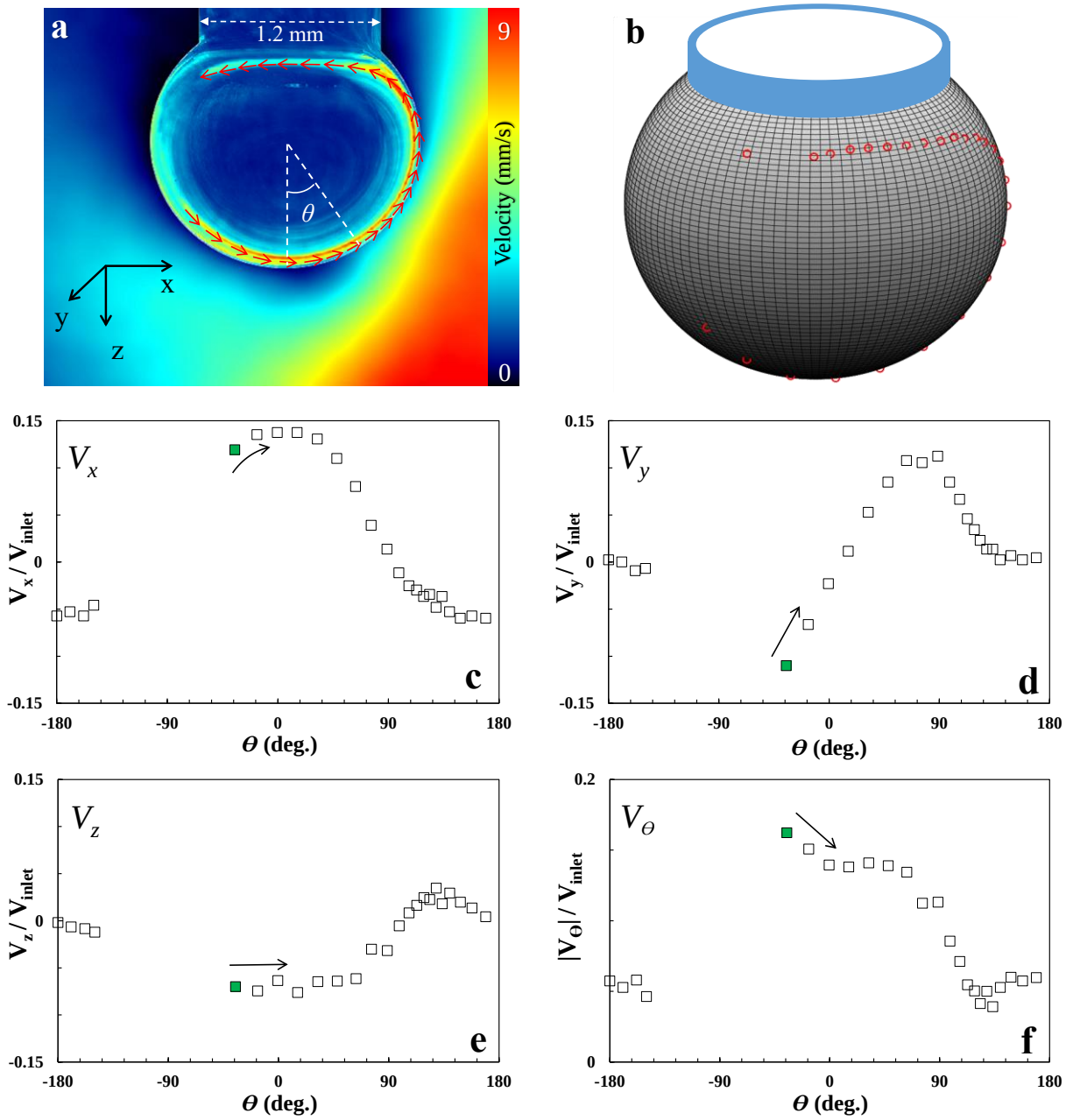

Figure 4. a) Particle movement at a bubble surface subjected to shear flow. b) Reconstructed 3D path of particles using equations 4 and 5. c)-f) Velocity components of the same particle group as a function of the polar angle θ.

In the next step, the effect of asymmetry on the rotational velocity of the interface is investigated. It is worth noting that the interfacial velocity is not constant at the bubble surface (c.f. Fig 4f). Hence, the speed of revolution ($\bar{\omega}$) is calculated as an average value, indicating the time required to complete at least one cycle of 2π. For asymmetry levels below 0.2 mm, $\bar{\omega}$ was too low to complete a cycle within the time of measurement; hence, we consider only the data for $\Delta x \geq 0.2$

mm. Fig 5 (violet squares) shows $\bar{\omega}$ of the particles at the interface (representing the velocity of the interface) as a function of the asymmetry. As can be seen from this figure, $\bar{\omega}$ increases with increasing asymmetry. Since the bulk flow structures between the experiments and simulations agreed well (cf. Sec. 3.2), we use the numerical results to calculate the net torque (Ω) (Fig. 5, unfilled triangles). This is the torque in y-direction, exerted by the liquid flow field onto the bubble surface, integrated over the full bubble surface. This quantity is not accessible in the experiments, because the employed PIV method does not capture the full three dimensional flow field around the bubble simultaneously. The net torque Ω was further employed to estimate the theoretical value of $\bar{\omega}$ for the bubble. The theoretical angular velocity (ω) of a solid sphere of radius R_s rotating in a quiescent fluid with viscosity μ_f is given in [42].

$$\Omega = 8\pi\mu_f R_s^3 \omega \tag{6}$$

Comparing this relation with our numerically calculated net torque yields a theoretical speed of revolution that is plotted in Figure 5 as well. Although the speed of revolution increases with the level of asymmetry in both experiment and simulation, the experimental $\bar{\omega}$ values are significantly smaller than the theoretically estimated ones (ω). Beside the slight differences in the bulk flow field, the deviation presumably results from three contributions. Firstly, the capillary prevents the free rotation underlying equation 6. Secondly, despite the low Reynolds number in the order of 1, the nozzle flow and the solid body rotation flow might not be perfectly superpositionable. Thirdly, the bubble interface does not act as a solid body but has fluidic/elastic properties.

3.4. *Estimation of shear stress and surface concentration of surfactant*

To shed light on the mechanisms underlying the observed interfacial flow, we investigate the shear stress and the concentration distribution on the bubble surface. For that purpose, the tangential velocity component V_θ at the bubble surface and at its boundary layer is extracted from the PTV/PIV measurements. The surface velocity is known from the tracking of adsorbed particles at the bubble surface (cf. Fig. 4) and the boundary layer velocity denotes the closest bulk PIV velocity vector adjacent to the bubble surface. Fig. 6a shows the surface velocity over the polar angle θ for 1 mm asymmetry in presence of 2.2 mM SDBS. Note, that this investigation does not consider the complete three-dimensional interface of the bubble but only the center plane (y=0) of the bubble. Here, positive values point in counterclockwise direction. Since the PIV measurements focus on the y=0 plane, we proceed with a two dimensional analysis. The gradient of V_θ at the bubble surface in normal direction is coupled to the tangential shear stress τ_θ

$$\tau_\theta\big|_{r=R_b} = \mu_f r \left.\frac{\partial (V_\theta / r)}{\partial r}\right|_{r=R_b} \tag{7}$$

where $\partial V_\theta/\partial r$ is approximated by the difference of the surface velocity to the closest bulk PIV velocity and their normal distance. The shear stress τ_θ at the interface (for the y=0 plane) is depicted in Fig. 6b (open squares) and compared to the wall shear stress from the corresponding simulations of a solid sphere at a needle tip (plus sign).

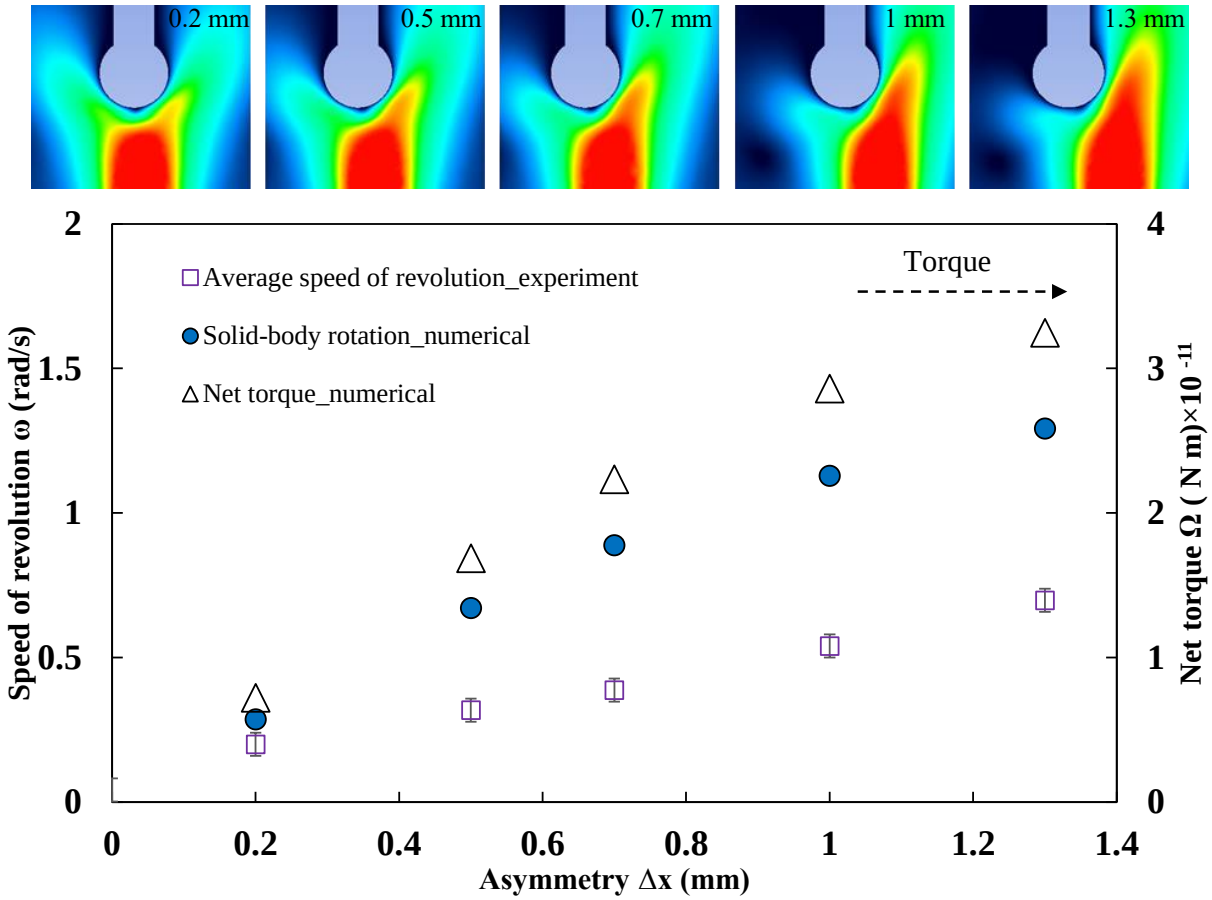

Figure 5. Speed of revolution as a function of asymmetry for an air bubble under shear flow. The solid-body angular velocity (ω, blue circles) was obtained using Eq. (6). The error bars estimate the variation of the speed of revolution between independent experimental runs. The top row of Fig. 5 shows the numerical flow field for each asymmetric configuration.

Fig. 6b displays two further simulations: the same asymmetric jet flow is exerted on a static solid sphere without needle (black crosses) and on a solid sphere with imposed constant rotation equal to ω=0.5 rad·s^{-1} (blue circles). As one can see, the shear stress for the stationary sphere is almost identical to the one with capillary because the capillary is placed in the wake of the flow where the velocities are almost zero. For the rotating sphere, the magnitude of the imposed velocity is adapted from the experimental results, i.e. $\omega \approx 0.5$ rad·s^{-1} for 1 mm asymmetry (see Fig. 5). As can be seen from Fig. 6b, the rotation only leads to slight differences in the wall shear stress. This again emphasizes that the slow rotation observed in the experiment does not change the wall shear stress considerably. Hence, the order of magnitude of the torque that has been calculated numerically should be within the range of the experiment.

Finally, to estimate the concentration distribution of the adsorbed surfactant on the interface along the center plane (y=0), we employ the Marangoni shear stress balance

$$\tau_\theta = \frac{1}{R_b}\frac{\partial \sigma}{\partial \theta}. \qquad (8)$$

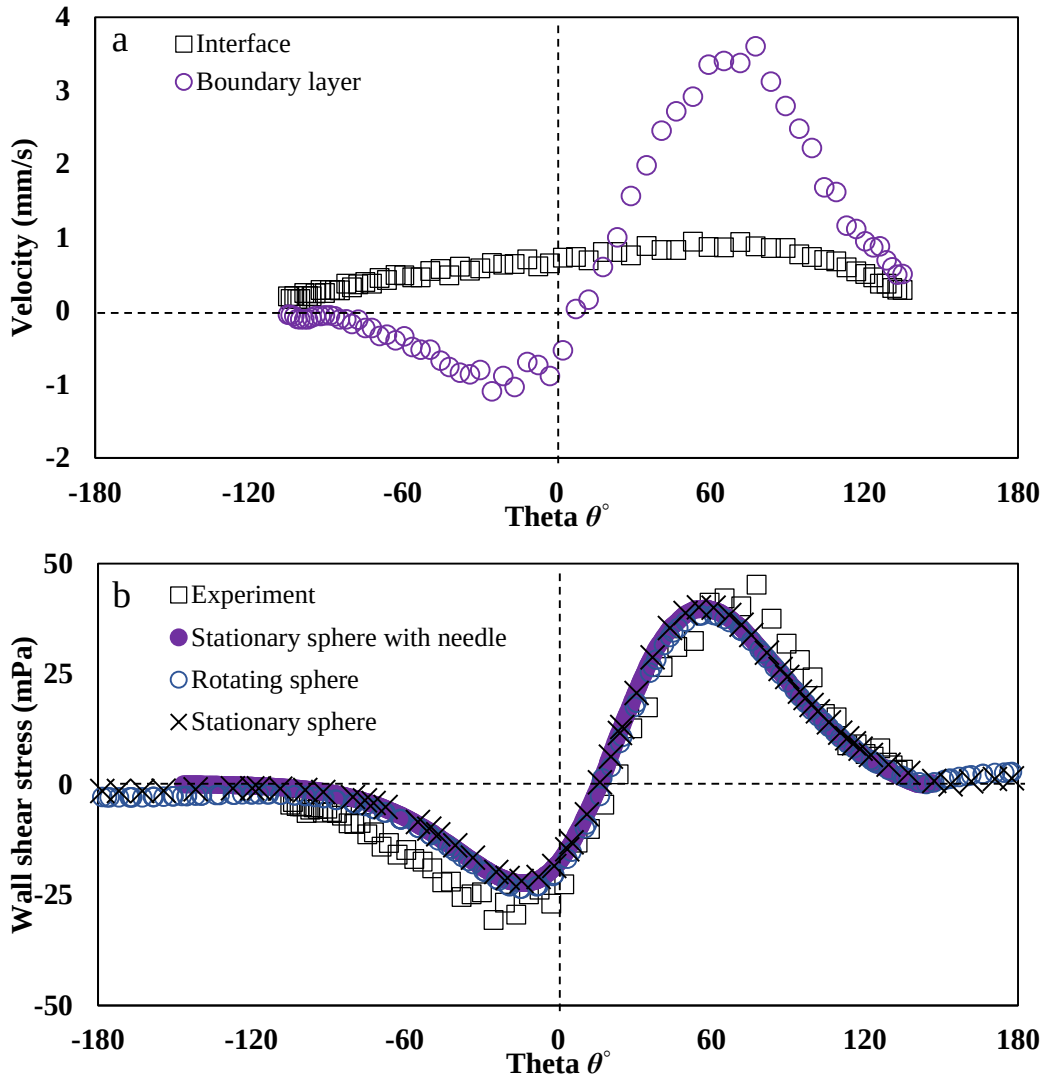

Figure 6. a) Tangential velocity distribution at bubble surface and its boundary layer for 1 mm asymmetry level. b) Wall shear stress is calculated from experimental velocity measurements using equation 7 and results of Fig. 6a, and from corresponding simulations of a solid sphere in an asymmetric flow field resting static on a needle (plus), resting static without needle (cross), and rotating (0.5 rad·s^{-1}, circle)

This equation assumes that the hydrodynamic stress is compensated by the Marangoni stress arising from the distribution of the surfactants at the interface. For a clean interface, there is no surface tension gradient and the surface flow follows the bulk flow. Thus, τ_θ must be zero, which is the above-mentioned condition for free-slip boundaries. Equation 8 has been widely used in the literature to calculate the distribution of surfactants at interfaces [13,14,43–46]. Once the dependence of σ on Γ is established, the surface concentration can be calculated using equations 7 and 8. According to Butler's equation, the surface tension relates to the bulk concentration as follows [32]:

$$\sigma_w - \sigma = \frac{\bar{R}T}{a}\ln\left[1+\frac{c^2}{4CMC^2}\exp\left[\frac{a}{\bar{R}T}\left(\sigma_w-\sigma_s\right)\right]\right] \quad (9)$$

where σ, σ_w and σ_s are the surface tension of surfactant solution, water and pure surfactant, respectively, a is the maximal partial molar area and *CMC* is the critical micelle concentration of the surfactant, $\bar{R}$ is the universal gas constant and T is the absolute temperature. The Gibbs isotherm for the surface concentration of ionic surfactants reads

$$\Gamma = -\frac{1}{2\bar{R}T}\frac{\partial\sigma}{\partial \ln c} \,. \tag{10}$$

Employing equations 9 and 10, equation 8 reduces to:

$$\tau_\theta = \frac{1}{R_b}\frac{\partial\sigma}{\partial\theta} = \frac{-\bar{R}T}{R_b(1-a\Gamma)}\frac{\partial\Gamma}{\partial\theta} \,. \tag{11}$$

The value of a (68 Å^2) is obtained by fitting the equation 9 (solid line in Fig. 2b) to the surface tension measurements plotted in Fig. 2b.

Once the value of a is known, the surface concentration can be calculated by discretizing the equation 11 along θ. Employing a forward differences approach yields

$$(\theta_{i+1}-\theta_i)(a\Gamma_i - 1)\left(\frac{R_p\tau_i}{\bar{R}T}\right) + \Gamma_i = \Gamma_{i+1} \,. \tag{12}$$

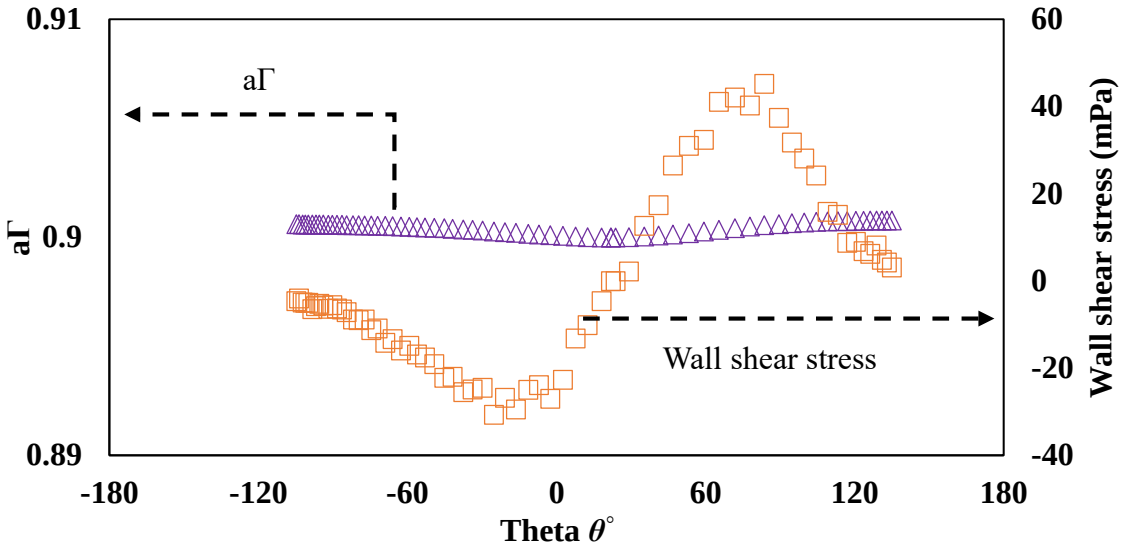

Figure 7. Hydrodynamic shear stress (orange squares) and surfactant distribution (purple triangles) calculated from experimental velocity measurements using equation 7 and 12.

Since the surfactant concentration in the shown measurements was around CMC, we estimate the interfacial concentration distribution for $a\cdot\Gamma = 0.9$ at the leading edge of the bubble (θ_1), i.e. we assume that 90% of the maximum concentration is reached there (note that this is just a hypothesis to illustrate the concentration distribution). As one can see from the calculations via equation 12, plotted in Fig. 7, the local surface coverage is only slightly modulated by the flow. This is due to the relatively small bulk velocity leading to stress magnitudes in the mPa range. Even minor surface tension gradients can compensate this weak shear. An example with distinct redistribution of the surfactant at higher bulk flow velocities is presented in the SI, Figure S3. However, the

hydrodynamic shear stress also shows that the conditions at the bubble in the asymmetric flow field essentially differ from the classical stagnant cap concept. In the symmetric flow case, the shear stress on the interface is free of curl and thus, can be compensated by Marangoni stress. However, the asymmetric shear has a rotational component ($\nabla\times\tau_m \neq 0$) that cannot be compensated by the Marangoni stress as Marangoni stress ($\tau_m \propto \nabla\Gamma$) results from the gradient of a scalar distribution (Γ) and thus, has to be free of curl ($\nabla\times\tau_m \propto \nabla\times\nabla\Gamma \equiv 0$). Hence, a rotational interfacial flow is induced in the asymmetric configuration and the adsorbed surfactant and PS particles are expected to circulate with the interfacial flow.

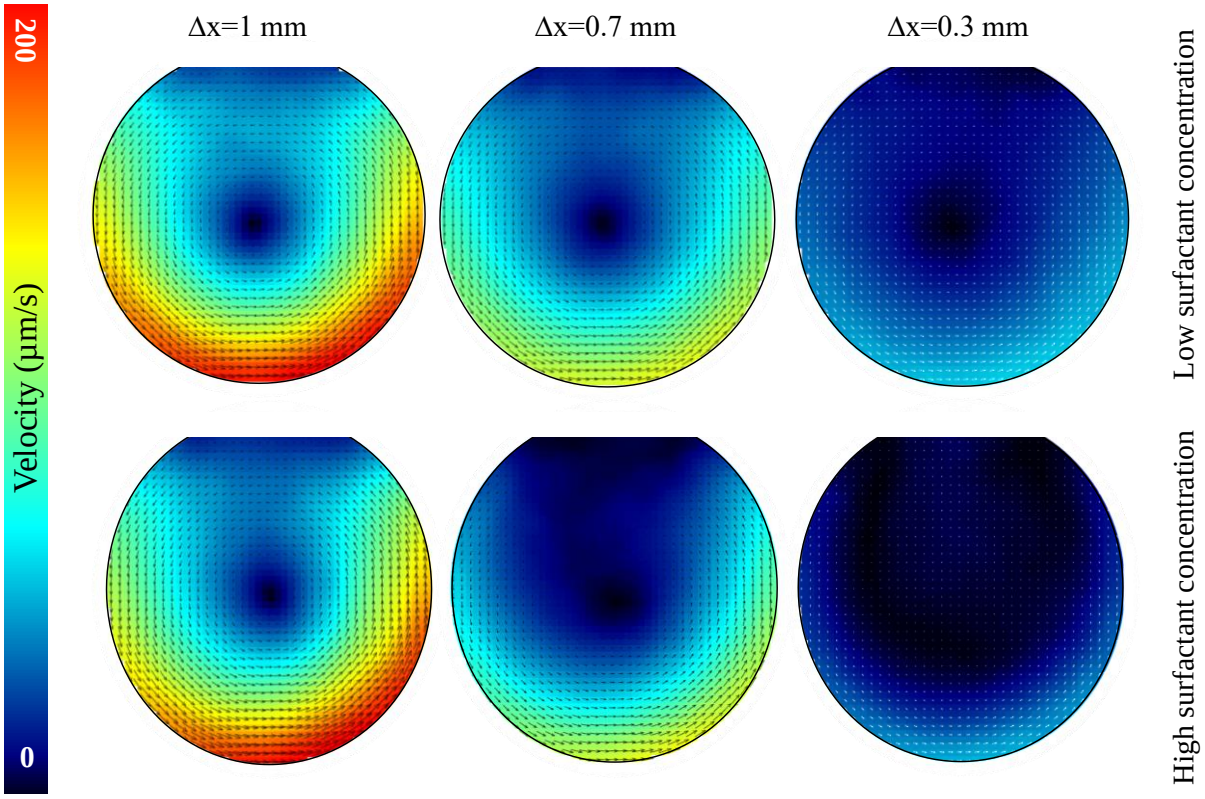

Figure 8. Circulating flow inside the droplet for different levels of asymmetry for 0.2 mM SDBS (upper) and 1.2 mM SDBS (lower) figures as measured by PIV.

3.5.*Internal flow pattern for a liquid-liquid system*

The flow pattern inside the air bubble cannot be resolved due to the experimental limitations associated with the tracer particle seeding in the gaseous phase. Hence, a liquid-liquid system was chosen to investigate the response of the interior fluid to the asymmetric flow field (video V3.mp4 in SI). The experiments were repeated in the same geometrical configuration using the refractive index matching fluids discussed in Section 2.1. To that end, a water-glycol droplet containing the SDBS surfactant was submerged into the silicone oil. The PS particles were dispersed in the polar medium (water-glycerol droplet) and then the droplet was placed in the asymmetric shear flow, which again provides a defined asymmetric shear level on the droplet interface similar to the bubble case. Only due to the changed viscosities of the solutions, the Reynolds number and thus the flow

pattern differed from the bubble experiments. Fig. 8 shows the internal velocity field at center plane i.e. y=0 depending on the degree of asymmetry for 0.2 mM SDSB and 1.2 mM SDBS. As it can be seen from this figure, the internal circulation is intensified for both cases with growing shear rate. For low surfactant concentration, higher velocity magnitudes are measured.

Discussion

To provide a sound interpretation of the described observations, we discuss the experimental limitations, which typically have to be considered in the study of interfacial phenomena. Before the flow measurements can be started, at least several minutes of waiting time are necessary to attach enough PS particles at the interface for particle tracking. This can introduce impurities to the system either from the surrounding atmosphere, construction parts, or due to the dissolution of rhodamine which is contained in the PS particles. Consequently, this technique at its current stage does not allow to investigate fresh and clean interfaces.

Furthermore, we note that the observed interfacial flow differs from the re-mobilization of the interface at high surfactant concentration and fast sorption kinetics which is reported in [47]. This re-mobilization happens when molecules freely desorb at the trailing edge and instantly adsorb at the leading edge. Hence, if the surfactant mass transfer is fast enough, a uniform surface concentration is obtained that is in equilibrium with the surrounding bulk phase. For bulk concentrations above CMC, the existing micelles can provide the required permanent material exchange (given that the kinetic processes are likewise fast enough). The resulting constant surface concentration excludes Marangoni stresses and remobilizes the interface. This is contrasted by our observation of a no-slip bubble surface and the downwards interfacial flow which opposes the upwards bulk flow. Furthermore, the circulating interfacial flow also was observed at concentrations well below CMC, which rejects the possibility of re-mobilization.

Additionally, we address the concentration dependence of the flow velocity observed for the case of a liquid-liquid system. Unlike the bubble experiments, a decrease in magnitude of the internal flow and thus the interfacial flow was obtained with increasing surfactant concentration. However, higher surfactant concentrations also lead to a more elongated shape of the pendant drop which interferes with the effect of the surfactant concentration on the surface velocity. For such elongated shapes, the lateral extension of the drop is smaller and thus the shear rate decreases in comparison to the low concentration case. Hence, to clearly analyze the effect of surfactant concentration on the interfacial and internal flow, further extensive experiments are necessary, e.g. with different surfactant types and buoyancy-matched phases.

Irrespective of these uncertainties, our experiments consistently show the existence of a circulating interfacial flow under asymmetric shear. For the first time, we experimentally visualize this phenomenon mainly known from theoretical studies before [28,48]. Our technique provides direct access to the hydrodynamic behavior of the bubble surface by tracking the velocity of the attached particles at the interface. This enabled us to reveal that the interface remains mobile even at high surfactant concentrations and to distinguish the circulating interfacial flow from a pure solid body rotation.

Based on the gained insights, Fig. 9 summarizes different scenarios for a surfactant-laden interface under dynamic conditions. For a rising bubble or a falling drop, the adsorbed material is swept to the trailing edge and the interfacial concentration at the leading edge decreases (Fig. 9a) [14]. The attached bubble at a capillary needle that is placed in a perfectly symmetric flow will behave similarly, i.e. the surfactant is swept upward and accumulates at the stagnation zone of the capillary (Fig. 9b). However, since minor deviations in the positioning of the bubble and the applied jet flow are always effective, this situation never was observed in our experiments. Only for a perfectly symmetric case, the resulting viscous stress on the interface is free of curl and can be fully compensated by Marangoni stresses. This symmetric case could then result in a vanishing interfacial velocity. The movement of adsorbed tracer particles under asymmetric shear shows that the response of the interface to the bulk flow leads to a continuous circulation of the bubble surface with a stagnant zone around the capillary (Fig. 9c). The rotational component of the shear flow at the bubble interface redistributes the surfactant, thereby remobilizing the interface [27,49,50]. In this case, a pronounced velocity gradient exists at the bubble surface with zero velocity near the capillary as seen in Fig. 6a. This distinguishes the interfacial flow under asymmetric shear from a solid body-like rotation, despite their visual resemblance. Fig. 9d schematically sketches the interfacial flow around the capillary from top view.

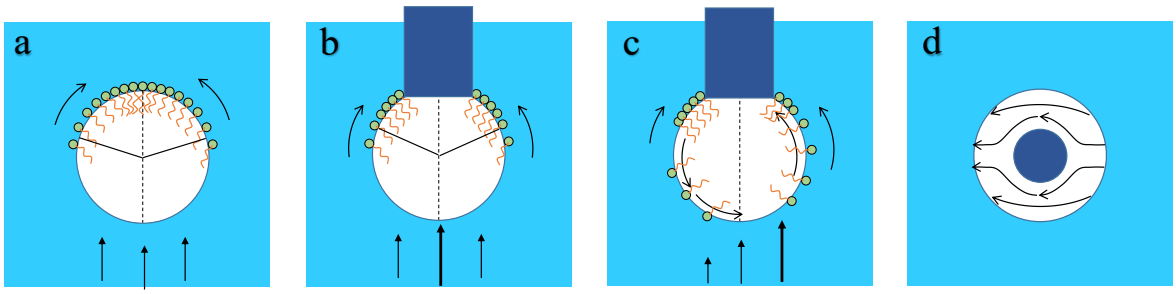

Figure 9. Schematic illustrating the surfactant distribution and shear forces for (a) a falling drop, (b) bubble in symmetric flow, (c) bubble in asymmetric flow in front view. (d) Flow field around the capillary in top view.

Conclusion and outlook

This study presents a direct experimental observation of the circulating interfacial flow [27,28,48–50] which occurs at a bubble under asymmetric shear flow in presence of the surfactant SDBS. Particle image velocimetry and particle tracking velocimetry (PIV/PTV) of adsorbed tracer particles is applied to investigate the flow structure and its magnitude. Extrapolation from bulk velocity measurements cannot fully capture the interfacial flow, which opposes the bulk flow on one side of the bubble, due to the limited spatial resolution and the high velocity gradients in the boundary layer. Instead, we tracked hydrophobic Polystyrene particles that are adsorbed directly at the interface of the bubble. Generally, for the tracking of adsorbed tracer particles, the influence of velocity gradients normal to the interface is restricted by the spatial extension of the particles, i.e. a few micrometers. Thus, our approach allows imaging the interfacial flow with sufficient accuracy.

A combined experimental and numerical characterization of the hydrodynamic shear acting on the bubble surface in asymmetric flow underlines the differences to the interfacial dynamics of

bubbles rising in quiescent liquid. In the symmetric flow, the Marangoni stresses resulting from the nonuniform distribution of the surfactants can counteract the viscous shear stress and cause immobility of the interface [2,51,52]. Under asymmetric shear flow, the interface remains mobile even at high surfactant concentrations. This impacts the interaction between the bubble surface and approaching or detaching bubbles or particles in technological applications [53]. Furthermore, knowledge on the interfacial flow allows to better understand and control phenomena like lateral bubble migration or the orientation of adsorbed anisotropic material. Our insights further are relevant for the modelling of adsorption-desorption processes, and general mass transfer operations (e.g. for dissolving gas bubbles) which are affected by the interfacial flow. Asymmetric shear can be caused by wall effects, interactions between the dispersed entities, or the flow structure of the continuous phase. Since these conditions apply for various reactors, our findings are significant for a broad range of applications in chemical and minerals engineering.

To approach the technological conditions, i.e. bubbles with Reynolds numbers in the order of 100 and higher, the interfacial particle tracking can be extended to rising or falling drops and bubbles in asymmetric shear flow. This requires an advanced measurement strategy, e.g. a camera moving with the rising bubble. If it is possible to perform bulk PIV measurements in parallel to PTV in the interface, comprehensive information on the hydrodynamic behavior of the moving bubbles and drops can be obtained. Further, our model configuration of a buoyant bubble (or a pendant drop for the liquid-liquid case) can be adapted to a precisely symmetric flow configuration. This could be achieved by employing a flow channel with a homogeneous flow field to eliminate the influence of small misalignments and to provide higher flow rates.

Acknowledgement

The authors would like to thank Prof. Aliyar Javadi and Aleksandr Bashkatov for their help in preliminary screening experiments of the system. Funding by the European Union's Horizon 2020 research and innovation program under grant agreement No 821265 is gratefully acknowledged. Furthermore, we acknowledge the financial support provided by the German Helmholtz Association.

Supplementary material

Electronic supplementary information (ESI) available. The flow pattern is shown for different concentration of SDBS. Additionally, the numerically calculated velocity distribution around the attached bubble for the case of free slip is reported. Finally, the wall shear stress and surfactant distribution for higher velocities are calculated numerically and plotted.

Videos showing the movement of PS particles at the bubble surface, the interfacial flow of the bubble as well as the internal circulation of the drop under shear flow are available.

References

1. Megaridis CM, Hodges JT, Xin J, Presser C, Day JM. Internal droplet circulation induced by surface-driven rotation. *Int J Heat Fluid Flow*. 2003;15(5):364-377. doi:10.1016/0142-727x(94)90050-7

2. Hosokawa S, Hayashi K, Tomiyama A. Evaluation of adsorption of surfactant at a moving

interface of a single spherical drop. *Exp Therm Fluid Sci*. 2018;96(September 2017):397-405. doi:10.1016/j.expthermflusci.2018.03.026

3. Alves SS, Orvalho SP, Vasconcelos JMT. Effect of bubble contamination on rise velocity and mass transfer. *Chem Eng Sci*. 2005;60(1):1-9. doi:10.1016/j.ces.2004.07.053

4. He Y, Yazhgur P, Salonen A, Langevin D. Adsorption-desorption kinetics of surfactants at liquid surfaces. *Adv Colloid Interface Sci*. 2015;222:377-384. doi:10.1016/j.cis.2014.09.002

5. Liggieri L, Ferrari M, Mondelli D, Ravera F. Surface rheology as a tool for the investigation of processes internal to surfactant adsorption layers. *Faraday Discuss*. 2005;129:125-140. doi:10.1039/b405538a

6. Karbaschi M, Bastani D, Javadi A, et al. Drop profile analysis tensiometry under highly dynamic conditions. *Colloids Surfaces A Physicochem Eng Asp*. 2012;413:292-297. doi:10.1016/j.colsurfa.2012.04.027

7. Miller R, Fainerman VB, Makievski A V., et al. Dynamics of protein and mixed protein/surfactant adsorption layers at the water/fluid interface. *Adv Colloid Interface Sci*. 2000;86(1):39-82. doi:10.1016/S0001-8686(00)00032-4

8. Defay R, Prigogine I, Bellemans A, Everett DH. *Surface Tension and Adsorption*. Longmans; 1966. https://books.google.de/books?id=5RBRAAAAMAAJ.

9. Barnes HA. Rheology of emulsions - a review. *Colloids Surfaces A Physicochem Eng Asp*. 1994;91(C):89-95. doi:10.1016/0927-7757(93)02719-U

10. Eastoe J, Dalton JS. Dynamic surface tension and adsorption mechanisms of surfactants at the air–water interface. *Adv Colloid Interface Sci*. 2000;85(2):103-144. doi:https://doi.org/10.1016/S0001-8686(99)00017-2

11. Miller R, Aksenenko E V, Fainerman VB. Dynamic interfacial tension of surfactant solutions. *Adv Colloid Interface Sci*. 2017;247:115-129. doi:10.1016/j.cis.2016.12.007

12. Lotfi M, Bastani D, Ulaganathan V, Miller R, Javadi A. Bubble in flow field: A new experimental protocol for investigating dynamic adsorption layers by using capillary pressure tensiometry. *Colloids Surfaces A Physicochem Eng Asp*. 2014;460:369-376. doi:10.1016/j.colsurfa.2013.11.011

13. Dukhin SS, Kovalchuk VI, Gochev GG, et al. Dynamics of Rear Stagnant Cap formation at the surface of spherical bubbles rising in surfactant solutions at large Reynolds numbers under conditions of small Marangoni number and slow sorption kinetics. *Adv Colloid Interface Sci*. 2015;222:260-274. doi:10.1016/j.cis.2014.10.002

14. Dukhin SS, Lotfi M, Kovalchuk VI, Bastani D, Miller R. Dynamics of rear stagnant cap formation at the surface of rising bubbles in surfactant solutions at large Reynolds and Marangoni numbers and for slow sorption kinetics. *Colloids Surfaces A Physicochem Eng Asp*. 2016;492:127-137. doi:10.1016/j.colsurfa.2015.12.028

15. Hosokawa S, Masukura Y, Hayashi K, Tomiyama A. Experimental evaluation of Marangoni stress and surfactant concentration at interface of contaminated single spherical drop using spatiotemporal filter velocimetry. *Int J Multiph Flow*. 2017;97:157-167.

doi:10.1016/j.ijmultiphaseflow.2017.08.007

16. Fukuta M, Takagi S, Matsumoto Y. Numerical study on the shear-induced lift force acting on a spherical bubble in aqueous surfactant solutions. *Phys Fluids*. 2008;20(4). doi:10.1063/1.2911040

17. Eggleton CD, Pawar YP, Stebe KJ. Insoluble surfactants on a drop in an extensional flow: A generalization of the stagnated surface limit to deforming interfaces. *J Fluid Mech*. 1999;385:79-99. doi:10.1017/S0022112098004054

18. Shi P, Rzehak R. Lift forces on solid spherical particles in wall-bounded flows. *Chem Eng Sci*. 2020;211:115264. doi:10.1016/j.ces.2019.115264

19. Pesci C, Weiner A, Marschall H, Bothe D. Computational analysis of single rising bubbles influenced by soluble surfactant. *J Fluid Mech*. 2018;856:709-763. doi:10.1017/jfm.2018.723

20. Zholkovskij EK, Koval'Chuk VI, Dukhin SS, Miller R. Dynamics of rear stagnant cap formation at low Reynolds numbers. 1. Slow sorption kinetics. *J Colloid Interface Sci*. 2000;226(1):51-59. doi:10.1006/jcis.2000.6786

21. Wegener M, Fevre M, Paschedag AR, Kraume M. Impact of Marangoni instabilities on the fluid dynamic behaviour of organic droplets. *Int J Heat Mass Transf*. 2009;52(11-12):2543-2551. doi:10.1016/j.ijheatmasstransfer.2008.11.022

22. Wegener M, Paschedag AR. The effect of soluble anionic surfactants on rise velocity and mass transfer at single droplets in systems with Marangoni instabilities. *Int J Heat Mass Transf*. 2012;55(5-6):1561-1573. doi:10.1016/j.ijheatmasstransfer.2011.11.011

23. Parkinson L, Sedev R, Fornasiero D, Ralston J. The terminal rise velocity of 10-100 μm diameter bubbles in water. *J Colloid Interface Sci*. 2008;322(1):168-172. doi:10.1016/j.jcis.2008.02.072

24. Takagi S, Matsumoto Y. Surfactant effects on bubble motion and bubbly flows. *Annu Rev Fluid Mech*. 2011;43:615-636. doi:10.1146/annurev-fluid-122109-160756

25. Shi P, Rzehak R, Lucas D, Magnaudet J. Hydrodynamic forces on a clean spherical bubble translating in a wall-bounded linear shear flow. *Phys Rev Fluids*. 2020;5(7):1-38. doi:10.1103/PhysRevFluids.5.073601

26. Takagi S, Ogasawara T, Fukuta M, Matsumoto Y. Surfactant effect on the bubble motions and bubbly flow structures in a vertical channel. *Fluid Dyn Res*. 2009;41(6). doi:10.1088/0169-5983/41/6/065003

27. Vlahovska PM, Bławzdziewicz J, Loewenberg M. Small-deformation theory for a surfactant-covered drop in linear flows. *J Fluid Mech*. 2009;624:293-337. doi:10.1017/S0022112008005417

28. Hanna JA, Vlahovska PM. Surfactant-induced migration of a spherical drop in Stokes flow. *Phys Fluids*. 2010;22(1):013102. doi:10.1063/1.3277665

29. Wright SF, Zadrazil I, Markides CN. *A Review of Solid–Fluid Selection Options for Optical-Based Measurements in Single-Phase Liquid, Two-Phase Liquid–Liquid and*

Multiphase Solid–Liquid Flows. Vol 58. Springer Berlin Heidelberg; 2017. doi:10.1007/s00348-017-2386-y

30. Sheely ML. Glycerol Viscosity Tables. *Ind Eng Chem*. 1932;24(9):1060-1064. doi:10.1021/ie50273a022

31. Aveyard R, Binks BP, Fletcher PDI, Rutherford CE. Measurement of contact angles of spherical monodisperse particles with surfactant solutions. *Colloids Surfaces A Physicochem Eng Asp*. 1994;83(1):89-98. doi:10.1016/0927-7757(93)02671-Z

32. Eftekhari M, Schwarzenberger K, Javadi A, Eckert K. The influence of negatively charged silica nanoparticles on the surface properties of anionic surfactants: Electrostatic repulsion or the effect of ionic strength? *Phys Chem Chem Phys*. 2020;22(4):2238-2248. doi:10.1039/c9cp05475h

33. Lau TCW, Nathan GJ. The effect of Stokes number on particle velocity and concentration distributions in a well-characterised, turbulent, co-flowing two-phase jet. *J Fluid Mech*. 2016;809:72-110. doi:10.1017/jfm.2016.666

34. Schneiders JFG, Scarano F, Elsinga GE. Resolving vorticity and dissipation in a turbulent boundary layer by tomographic PTV and VIC+. *Exp Fluids*. 2017;58(4):1-14. doi:10.1007/s00348-017-2318-x

35. Bahramian A, Thomas RK, Penfold J. The adsorption behavior of ionic surfactants and their mixtures with nonionic polymers and with polyelectrolytes of opposite charge at the air-water interface. *J Phys Chem B*. 2014;118(10):2769-2783. doi:10.1021/jp500672f

36. Bahramian A, Zarbakhsh A. Interfacial equation of state for ionized surfactants at oil/water interfaces. *Soft Matter*. 2015;11(32):6482-6491. doi:10.1039/c5sm01406a

37. Lin S-Y, Wang W-J, Lin L-W, Chen L-J. Systematic effects of bubble volume on the surface tension measured by pendant bubble profiles. *Colloids Surfaces A Physicochem Eng Asp*. 1996;114:31-39. doi:https://doi.org/10.1016/0927-7757(96)03527-3

38. Lin SY, Chen LJ, Xyu JW, Wang WJ. An Examinaiion on the Accuracy of Interfacial Tension Measurement from Pendant Drop Profiles. *Langmuir*. 1995;11(10):4159-4166. doi:10.1021/la00010a084

39. Fainerman VB, Kovalchuk VI, Aksenenko E V., Miller R. Dilational Viscoelasticity of Adsorption Layers Measured by Drop and Bubble Profile Analysis: Reason for Different Results. *Langmuir*. 2016;32(22):5500-5509. doi:10.1021/acs.langmuir.6b01134

40. Tzounakos A, Karamanev DG, Margaritis A, Bergougnou MA. Effect of the surfactant concentration on the rise of gas bubbles in power-law non-Newtonian liquids. *Ind Eng Chem Res*. 2004;43(18):5790-5795. doi:10.1021/ie049649t

41. Pawliszak P, Ulaganathan V, Bradshaw-Hajek BH, Manica R, Beattie DA, Krasowska M. Mobile or Immobile? Rise Velocity of Air Bubbles in High-Purity Water. *J Phys Chem C*. 2019;123(24):15131-15138. doi:10.1021/acs.jpcc.9b03526

42. Feuillebois F, Lasek A. On the rotational historic term in non-stationary stokes flow. *Q J Mech Appl Math*. 1978;31(4):435-443. doi:10.1093/qjmam/31.4.435

43. Kovalchuk NM, Kovalchuk VI, Vollhardt D. Numerical study of the Marangoni instability resulting in surface tension auto-oscillations: General regularities of the system evolution. *Phys Rev E - Stat Physics, Plasmas, Fluids, Relat Interdiscip Top*. 2001;63(3):1-10. doi:10.1103/PhysRevE.63.031604

44. Fleckenstein S, Bothe D. Simplified modeling of the influence of surfactants on the rise of bubbles in VOF-simulations. *Chem Eng Sci*. 2013;102:514-523. doi:https://doi.org/10.1016/j.ces.2013.08.033

45. Ahmed Z, Izbassarov D, Lu J, Tryggvason G, Muradoglu M, Tammisola O. Effects of soluble surfactant on lateral migration of a bubble in a pressure driven channel flow. *Int J Multiph Flow*. 2020;126:103251. doi:10.1016/j.ijmultiphaseflow.2020.103251

46. Piedfert A, Lalanne B, Masbernat O, Risso F. Numerical simulations of a rising drop with shape oscillations in the presence of surfactants. *Phys Rev Fluids*. 2018;3(10):1-22. doi:10.1103/PhysRevFluids.3.103605

47. Stebe KJ, Lin SY, Maldarelli C. Remobilizing surfactant retarded fluid particle interfaces. I. Stress-free conditions at the interfaces of micellar solutions of surfactants with fast sorption kinetics. *Phys Fluids A*. 1991;3(1):3-20. doi:10.1063/1.857862

48. Blawzdziewicz J, Vlahovska P, Loewenberg M. Rheology of a dilute emulsion of surfactant-covered spherical drops. *Phys A Stat Mech its Appl*. 2000;276(1):50-85. doi:10.1016/S0378-4371(99)00366-0

49. Mandal S, Das S, Chakraborty S. Effect of Marangoni stress on the bulk rheology of a dilute emulsion of surfactant-laden deformable droplets in linear flows. *Phys Rev Fluids*. 2017;2(11):1-29. doi:10.1103/PhysRevFluids.2.113604

50. Lee J, Pozrikidis C. Effect of surfactants on the deformation of drops and bubbles in Navier-Stokes flow. *Comput Fluids*. 2006;35(1):43-60. doi:10.1016/j.compfluid.2004.11.004

51. Nock WJ, Heaven S, Banks CJ. Mass transfer and gas-liquid interface properties of single CO2 bubbles rising in tap water. *Chem Eng Sci*. 2016;140:171-178. doi:10.1016/j.ces.2015.10.001

52. Palaparthi R, Papageorgiou DT, Maldarelli C. Theory and experiments on the stagnant cap regime in the motion of spherical surfactant-laden bubbles. *J Fluid Mech*. 2006;559(December 2013):1-44. doi:10.1017/S0022112005007019

53. Sommer AE, Nikpay M, Heitkam S, Rudolph M, Eckert K. A novel method for measuring flotation recovery by means of 4D particle tracking velocimetry. *Miner Eng*. 2018;124(April):116-122. doi:10.1016/j.mineng.2018.05.006